


Mode-coupled perturbation growth on the interfaces of cylindrical implosion: A comparison between theory and experiment

Xinyu Zhang ¹, Shuai Zhang ¹, Zixiang Yan ², Huiling Duan ^{1,*}, Yongkun Ding ³, and Wei Kang ^{1,†}

¹*HEDPS, Center for Applied Physics and Technology, and College of Engineering, Peking University, Beijing 100871, China*

²*School of Science, Beijing University of Posts and Telecommunications, Beijing 100876, China*

³*Institute of Applied Physics and Computational Mathematics, Beijing 100094, China*

 (Received 10 August 2023; revised 22 January 2024; accepted 16 February 2024; published 5 March 2024)

We present a mode-coupled weakly nonlinear model for the evolution of perturbations on cylindrical multilayered shells in a decelerating implosion. We show that nonlinear mode-mode interactions among large wave-number fundamental modes are able to induce the growth of small wave number harmonic modes, i.e., forming inverse cascade channels in the wave-number space. When uniform compression and interfacial coupling are taken into consideration, the amplitude of some perturbation modes exhibits an oscillatory growth pattern, which is beyond the intuition that perturbation amplitudes usually have a fast growth tendency in an implosion dominated by the Bell-Plesset effect. Our model accounts well for the previous experiments of Hsing *et al.* [Hsing *et al.*, *Phys. Rev. Lett.* **78**, 3876 (1997) and *Phys. Plasmas* **4**, 1832 (1997)], which is among the few experiments of multimode multiinterface perturbation development in a cylindrical implosion. In particular, we find that the inverse cascade of modes is the origin of the excitation and growth of the wave number $k = 2$ harmonic mode on the inner interface. The observed decrease of the fundamental modes on the inner interface is mainly attributed to the decreasing period of the oscillatory growth process. These results may afford further insight into the distortion of hot spots in inertial confined fusion implosion near the final stage, and also help to design multimode perturbation experiments in converging geometry in the coming future.

DOI: [10.1103/PhysRevE.109.035203](https://doi.org/10.1103/PhysRevE.109.035203)

I. INTRODUCTION

Hydrodynamic instability, especially the Rayleigh-Taylor (RT) instability [1–3], is one of the major concerns in inertial confined fusion (ICF) [4–9] and evolution of stars [10–12]. For a multilayered ICF target [13,14], hydrodynamic instability is significant at both acceleration and deceleration phases of implosion, taking place near the outer and inner interfaces of the fuel layer, respectively [15,16]. A profound consequence of this instability [17–19] is that it triggers symmetry breaking of the hot spot, resulting in severe mixing of cold components and hot fuel [20,21], and thus leads to a significant reduction of core temperature. It has been long conjectured that hydrodynamic instability is somehow underestimated in theories with some important physical factors not well taken into consideration, as has been observed in experiments that overall fusion yields [16,22] are systematically lower than those predicted by theoretical and numerical calculations.

This inconsistency has motivated consecutive efforts from both theoretical and experimental sides. Theoretical investigations have been focused on taking various physical effects into consideration, including interfacial coupling [23–31], mode coupling [32–35], compressibility [36–38], and even the effect of magnetic fields [29,39–42]. These theoretical models

afford qualitative physical pictures from different perspectives. However, it is still desirable to know which among these effects are essential to account for experimental findings. On the other side, corresponding experimental efforts have been devoted to the improvements of diagnostics and designs of experiments to provide discriminative experimental evidence to assess the influence of various physical factors. These include experiments based on the implosion platform of cylindrical geometry, where high-quality images of distorted shells are relatively easy to obtain [43–52], and are still essential to the geometric contraction effect, i.e., the Bell-Plesset (BP) effect [53,54], is well exhibited. In this context, it becomes attractive to have a theoretical model in addition to direct numerical simulations, which contains minimum necessary physical factors simultaneously, to account for available experiments and to guide the design of future experiments. In this way, one may have a better chance to gain further insight into the roles played by various physical factors in the instability growth in implosion processes.

In general, perturbations on a cylindrical interface can be decomposed into a series of sine and cosine components (modes). Note that the development of perturbations on the cylindrical axial direction is not considered here, and thereby the evolution of perturbations on the cylindrical interfaces is actually reduced to a two-dimensional problem. Nonlinear development of a given mode, e.g., the formation of bubbles and spikes, as well as the interaction between various modes, are two general features of nonlinear evolution of perturbations on cylindrical interfaces. Both of them contribute to the

*hlduan@pku.edu.cn

†weikang@pku.edu.cn

probable turbulent mixing [55–58]. However, for cylindrical implosion systems, most works so far have focused on the nonlinear development of a single-mode initial perturbation [45–52,59–64]. Theoretical modeling and experimental measurements of nonlinear interactions between different modes in cylindrical implosion or contraction are rarely reported [43,44], partly because of the huge difficulties encountered in theoretical analyses and experimental realizations. A theoretical analysis that takes into consideration interactions between modes is thus of great help to reveal important physical features in the evolution of multimode perturbations on cylindrical interfaces, and may also afford immediate support to the design of prospective multimode experiments in cylindrical implosions of multi-interfaces.

In this paper, we present a mode-coupled weakly nonlinear model with uniform compression for the evolution of perturbations on cylindrical multilayered shells in a decelerating implosion. We show that the nonlinear mode-mode interaction among large wave-number fundamental modes is able to induce the growth of small wave-number harmonic modes, i.e., forming an inverse cascade in the wave-number space. In addition, when uniform compression and interfacial coupling are taken into consideration, the amplitude of some perturbation modes exhibits an oscillatory growth pattern, which is beyond the intuition that perturbation amplitudes usually have a fast growth tendency in an implosion dominated by the BP effect. A careful comparison with the experiments of Hsing *et al.* [43,44] shows that our model well reproduces the evolution of perturbations before the arrival of the reflected shock wave from the cylindrical center. In particular, we find that the inverse cascade of modes is the origin of the excitation and growth of the wave number $k = 2$ harmonic mode in the inner interface. The observed decrease in the perturbation amplitudes of fundamental modes on the inner interface is mainly attributed to the decreasing period of the oscillatory growth process. These features may afford further insight into the distortion of hot spots in ICF implosion near the final stage and also help to design multimode perturbation experiments in the coming future.

The rest of this paper is composed of three sections. In Sec. II, we show how to build the linear and third-order mode-coupled weakly nonlinear model based on the potential flow theory. A detailed comparison between calculation and experimental results [43] is provided in Sec. III and, finally, we conclude our work with a short summary in Sec. IV.

II. THEORETICAL MODEL

A. Implosion configuration and governing equations

The initial configuration of the multilayered cylindrical shells considered in our theoretical model is schematically displayed in Fig. 1, where a two-dimensional axisymmetric geometry is assumed. In accordance with the experiment [43,44], the whole system is composed of three different fluids with different densities, and thus denoted as 1, 2, and 3, respectively with increasing radius. The undisturbed radii of the inner and outer interfaces, which are time-dependent functions, are denoted as $R^i(t)$ and $R^o(t)$, respectively, and the symbol α is used to represent the ratio between $R^o(t)$

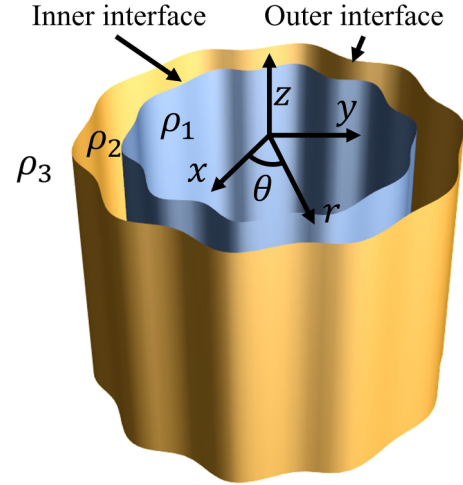


FIG. 1. Schematic illustration of the cylindrical shell. Two interfaces separate three fluids of density ρ_1 , ρ_2 , and ρ_3 . Azimuthal perturbations at the inner and outer interfaces are represented exaggeratedly.

and $R^i(t)$, i.e., $\alpha = R^o(t)/R^i(t)$, following previous works [30]. Disturbed inner and outer interfaces are then represented as azimuthal angle θ dependent functions as $r^{i,o}(\theta, t) = R^{i,o}(t) + \eta^{i,o}(\theta, t)$, where $r^{i,o}$ are the radial coordinates of interfaces and $\eta^{i,o}$ are azimuthal perturbations at the interfaces. Note that in the experiment [43], there was an additional ablation layer outside fluid 3. Before the experimental results started to be recorded, the perturbation amplitudes on the outer interface had been introduced by the perturbations on the ablation layer through coupling effects. However, during the recording period, which is also the calculation time interval of our model, the distance between the outer interface and the ablation layer increases rapidly because of the fast expansion of fluid 3, which makes the influence of the ablation layer on the outer interface diminish quickly. So, the model is simplified to the configuration displayed in Fig. 1 without including the ablation layer.

For irrotational, inviscid, and homogeneous fluids, the continuity equation $\frac{\partial \rho}{\partial t} + \nabla \cdot (\rho \mathbf{u}) = 0$ can be recast with velocity potential Φ as

$$\frac{1}{\rho} \frac{\partial \rho}{\partial t} = -\nabla \mathbf{u} = -\nabla^2 \Phi, \quad (1)$$

where Φ is defined by $\mathbf{u} = \nabla \Phi$, and ρ is the density. The potential function of the internal fluid is denoted as Φ_1 , the potential of the middle shell is Φ_2 , and the potential of the external fluid is Φ_3 . The compressibility can then be taken into account as a source of the potential function as [53]

$$\nabla^2 \Phi_n = F_n(t), \quad (2)$$

where $F_n(t) = -\dot{\rho}_n/\rho_n$ is the source term and $n = 1, 2$, and 3 for each fluid. The density of each fluid can also be determined as a function of $R^i(t)$ and $R^o(t)$ via the conservation law of mass, and so does $F_n(t)$. For the internal fluid, ρ_1 is determined by $\pi (R^i)^2 \rho_1(t) = \pi (R_{ini}^i)^2 \rho_1(0) = \text{const}$, while the middle shell obeys $\pi [(R^o(t))^2 - (R^i(t))^2] \rho_2(t) = \pi [(R^o(0))^2 - (R^i(0))^2] \rho_2(0) = \text{const}$. For the expanding outer fluid, the $F_3(t)$ is not determined through the

conservation law. Instead, it is inferred from the experimental finding that the Atwood number of the outer interface, defined as $A_i^o = (\rho_3 - \rho_2)/(\rho_3 + \rho_2)$, is approximately a constant around -0.15 , and whereby $F_3(t) \approx 2A_i^o/(A_i^o)^2 - 1 + F_2(t)$.

Following the notations of Ref. [30], the governing equations are expressed as

$$\begin{aligned} \frac{\partial \eta^s}{\partial t} + \frac{1}{r^2} \frac{\partial \eta^s}{\partial \theta} \frac{\partial \Phi_n}{\partial \theta} - \frac{\partial \Phi_n}{\partial r} \\ = \frac{\partial \eta^s}{\partial t} + \frac{1}{r^2} \frac{\partial \eta^s}{\partial \theta} \frac{\partial \Phi_{n+1}}{\partial \theta} - \frac{\partial \Phi_{n+1}}{\partial r} = -\dot{R}^s \\ \text{at } r = R^s + \eta^s, \end{aligned} \quad (3)$$

$$\begin{aligned} \rho_{n+1} \left[\frac{\partial \Phi_{n+1}}{\partial t} + \frac{1}{2} \left(\frac{\partial \Phi_{n+1}}{\partial r} \right)^2 + \frac{1}{2r^2} \left(\frac{\partial \Phi_{n+1}}{\partial \theta} \right)^2 \right] \\ - \rho_n \left[\frac{\partial \Phi_n}{\partial t} + \frac{1}{2} \left(\frac{\partial \Phi_n}{\partial r} \right)^2 + \frac{1}{2r^2} \left(\frac{\partial \Phi_n}{\partial \theta} \right)^2 \right] = 0 \\ \text{at } r = R^s + \eta^s, \end{aligned} \quad (4)$$

where s takes i for the inner interface and takes o for the outer interface. Note that in Eq. (4), n varies with s , so we have $n = 1$ for $s = i$ and $n = 2$ for $s = o$. There are two additional boundary conditions at the origin of the cylindrical coordinates and at infinite distance, i.e.,

$$\frac{1}{r} \frac{\partial \Phi_1}{\partial \theta} = 0 \quad \text{at } r \rightarrow 0, \quad (5a)$$

$$\frac{1}{r} \frac{\partial \Phi_3}{\partial \theta} = 0 \quad \text{at } r \rightarrow \infty \quad (5b)$$

Here Eq. (3) is actually the kinematic boundary condition, which describes the continuity of normal velocities across interfaces. Equation (4) is the dynamic boundary condition derived from the integral of the Bernoulli equation. Note that we have neglected the pressure inhomogeneity, which can be replaced by an equivalent interface perturbation when necessary [25]. Equations (5a) and (5b) account for the disappearance of perturbations at both $r \rightarrow 0$ and $r \rightarrow \infty$.

Following the experimental setup of Ref. [43], we consider perturbations composed of both cosine and sine modes, which implies that $\eta^{i,o} = \sum_m a_m \cos(m\theta) + b_m \sin(m\theta)$, where a_m and b_m are expansion coefficients with $m = 1, 2, 3, \dots$. The expansion of $\eta^{i,o}$ with two fundamental azimuthal modes, represented by k_1 and k_2 , respectively, can then be

expressed as

$$\begin{aligned} \eta^{i,o} = & \varepsilon \eta_{1,c1}^{i,o} \cos k_1 \theta + \varepsilon \eta_{1,c2}^{i,o} \cos k_2 \theta + \varepsilon^2 \eta_{2,o}^{i,o} \\ & + \varepsilon^2 \eta_{2,c1}^{i,o} \cos (k_1 + k_2) \theta + \varepsilon^2 \eta_{2,c2}^{i,o} \cos (k_1 - k_2) \theta \\ & + \varepsilon^2 \eta_{2,c3}^{i,o} \cos 2k_1 \theta + \varepsilon^2 \eta_{2,c4}^{i,o} \cos 2k_2 \theta \\ & + \varepsilon^3 \eta_{3,c1}^{i,o} \cos (2k_1 - k_2) \theta + \varepsilon^3 \eta_{3,c2}^{i,o} \cos (k_1 - 2k_2) \theta \\ & + \varepsilon^3 \eta_{3,c3}^{i,o} \cos k_1 \theta + \varepsilon^3 \eta_{3,c4}^{i,o} \cos k_2 \theta \\ & + \varepsilon^3 \eta_{3,c5}^{i,o} \cos (2k_1 + k_2) \theta + \varepsilon^3 \eta_{3,c6}^{i,o} \cos (k_1 + 2k_2) \theta \\ & + \varepsilon^3 \eta_{3,c7}^{i,o} \cos 3k_1 \theta + \varepsilon^3 \eta_{3,c8}^{i,o} \cos 3k_2 \theta \\ & + \varepsilon \eta_{1,s1}^{i,o} \sin k_1 \theta + \varepsilon \eta_{1,s2}^{i,o} \sin k_2 \theta \\ & + \varepsilon^2 \eta_{2,s1}^{i,o} \sin (k_1 + k_2) \theta + \varepsilon^2 \eta_{2,s2}^{i,o} \sin (k_1 - k_2) \theta \\ & + \varepsilon^2 \eta_{2,s3}^{i,o} \sin 2k_1 \theta + \varepsilon^2 \eta_{2,s4}^{i,o} \sin 2k_2 \theta \\ & + \varepsilon^3 \eta_{3,s1}^{i,o} \sin (2k_1 - k_2) \theta + \varepsilon^3 \eta_{3,s2}^{i,o} \sin (k_1 - 2k_2) \theta \\ & + \varepsilon^3 \eta_{3,s3}^{i,o} \sin k_1 \theta + \varepsilon^3 \eta_{3,s4}^{i,o} \sin k_2 \theta \\ & + \varepsilon^3 \eta_{3,s5}^{i,o} \sin (2k_1 + k_2) \theta + \varepsilon^3 \eta_{3,s6}^{i,o} \sin (k_1 + 2k_2) \theta \\ & + \varepsilon^3 \eta_{3,s7}^{i,o} \sin 3k_1 \theta + \varepsilon^3 \eta_{3,s8}^{i,o} \sin 3k_2 \theta + O(\varepsilon^4), \end{aligned} \quad (6)$$

where the parameter ε is used to indicate the order of perturbations only. The amplitudes of perturbations for various orders of ε are represented by $\eta_{\alpha,\beta}^{i,o}$ with two subscripts on the right-hand side of Eq. (6). The first subscript α denotes the order of perturbation with respect to ε , and the second subscript β represents the numeration of the term on the same order of ε . When they are coefficients of cosine terms, a prefix c is attached before the numeration and a prefix s is attached for sine terms. Note that the two fundamental azimuthal modes together with their couplings are all included in the expansions. To have a close comparison with experiments [43], we shall consider the mode $k_1 = 10$, corresponding to the premachined surface ripple, and the mode $k_2 = 4$ induced by laser imprinting in the discussions hereinafter.

B. Linear instability

By keeping the first-order terms of ε , the velocity potentials can be written in expansion forms as

$$\Phi_1 = \left[R^i \dot{R}^i - \frac{F_1}{2} (R^i)^2 \right] \ln r + \frac{r^2 F_1(t)}{4} + \varepsilon a_1(t) r^{k_1} \cos k_1 \theta + \varepsilon b_1(t) r^{k_2} \cos k_2 \theta + \varepsilon c_1(t) r^{k_1} \sin k_1 \theta + \varepsilon d_1(t) r^{k_2} \sin k_2 \theta, \quad (7)$$

$$\begin{aligned} \Phi_2 = & \left[R^i \dot{R}^i - \frac{F_2}{2} (R^i)^2 \right] \ln r + \frac{r^2 F_2(t)}{4} + \varepsilon a_2(t) r^{k_1} \cos k_1 \theta + \varepsilon b_2(t) r^{k_2} \cos k_2 \theta + \varepsilon c_2(t) r^{-k_1} \cos k_1 \theta + \varepsilon d_2(t) r^{-k_2} \cos k_2 \theta \\ & + \varepsilon e_2(t) r^{k_1} \sin k_1 \theta + \varepsilon f_2(t) r^{k_2} \sin k_2 \theta + \varepsilon g_2(t) r^{-k_1} \sin k_1 \theta + \varepsilon h_2(t) r^{-k_2} \sin k_2 \theta, \end{aligned} \quad (8)$$

$$\Phi_3 = \left[R^o \dot{R}^o - \frac{F_3}{2} (R^o)^2 \right] \ln r + \frac{r^2 F_3(t)}{4} + \varepsilon a_3(t) r^{-k_1} \cos k_1 \theta + \varepsilon b_3(t) r^{-k_2} \cos k_2 \theta + \varepsilon c_3(t) r^{-k_1} \sin k_1 \theta + \varepsilon d_3(t) r^{-k_2} \sin k_2 \theta, \quad (9)$$

where $a_1(t) - d_1(t)$, $a_2(t) - h_2(t)$, and $a_3(t) - d_3(t)$ are undetermined coefficients and will be expressed by the expansion form of η^s in Eq. (6).

When Eqs. (7)–(9) are inserted into Eqs. (3) and (4), linearized equations of η^i and η^o for mode k_1 , in terms of $\eta_{1,c1}^i$ and $\eta_{1,c1}^o$, can be arrived at as

$$\begin{aligned}
 & \overbrace{\ddot{\eta}_{1,c1}^i + 2\frac{\dot{R}^i}{R^i}\dot{\eta}_{1,c1}^i}^{\text{BP term}} + \overbrace{(1 - k_1 A_t^i)\frac{\ddot{R}^i}{R^i}\eta_{1,c1}^i}^{\text{RT term}} + k_1 \overbrace{\frac{\alpha^{2k_1-2}(\alpha^2 - 1)(A_t^i + 1)(A_t^o + 1)}{(\alpha^{2k_1} - 1)(\alpha^{2k_1} + A_t^i A_t^o)}\frac{\dot{R}^i}{R^i}\dot{\eta}_{1,c1}^i}^{\text{Thin-shell correction I}} + k_1 \overbrace{\frac{A_t^i A_t^o (A_t^i + 1)}{\alpha^{2k_1} + A_t^i A_t^o}\frac{\ddot{R}^i}{R^i}\eta_{1,c1}^i}^{\text{Thin-shell correction II}} \\
 & + k_1 \overbrace{\frac{\alpha^{2k_1-2}(\alpha^2 - 1)(A_t^i + 1)(A_t^o + 1)}{(\alpha^{2k_1} - 1)(\alpha^{2k_1} + A_t^i A_t^o)}\frac{(\dot{R}^i)^2}{(R^i)^2}\eta_{1,c1}^i}^{\text{Thin-shell correction III}} - k_1 \overbrace{\frac{\alpha^{3k_1-3}(\alpha^2 - 1)(A_t^i + 1)(A_t^o + 1)}{(\alpha^{2k_1} - 1)(\alpha^{2k_1} + A_t^i A_t^o)}\frac{(\dot{R}^i)^2}{(R^i)^2}\eta_{1,c1}^o}^{\text{Coupling term I}} \\
 & - k_1 \overbrace{\frac{\alpha^{k_1-1}(\alpha^2 - 1)(A_t^i + 1)(\alpha^{2k_1} + A_t^o)}{(\alpha^{2k_1} - 1)(\alpha^{2k_1} + A_t^i A_t^o)}\frac{\dot{R}^i}{R^i}\dot{\eta}_{1,c1}^o}^{\text{Coupling term II}} - k_1 \overbrace{\frac{\alpha^{k_1-1}(A_t^i + 1)A_t^o}{\alpha^{2k_1} + A_t^i A_t^o}\frac{\dot{R}^i}{R^i}\eta_{1,c1}^o}^{\text{Coupling term II}} \\
 & + \overbrace{\frac{(A_t^i - 1)(\alpha^{2k_1} - A_t^o)(\dot{F}_1 R^i + F_1 \dot{R}^i)}{2(\alpha^{2k_1} + A_t^i A_t^o)R^i}\eta_{1,c1}^i}^{\text{Compressibility term I}} - \overbrace{\frac{\alpha^{k_1-1}(A_t^i + 1)(A_t^o + 1)(\alpha^2 \dot{F}_3 R^i + F_3 \dot{R}^i)}{2(\alpha^{2k_1} + A_t^i A_t^o)R^i}\eta_{1,c1}^o}^{\text{Compressibility term I}} \\
 & + \overbrace{\frac{F_1(A_t^i - 1)(\alpha^{2k_1} - A_t^o)}{2(\alpha^{2k_1} + A_t^i A_t^o)}\dot{\eta}_{1,c1}^i}^{\text{Compressibility term II}} - \overbrace{\frac{F_3\alpha^{k_1+1}(A_t^i + 1)(A_t^o + 1)}{2(\alpha^{2k_1} + A_t^i A_t^o)}\dot{\eta}_{1,c1}^o}^{\text{Compressibility term II}} \\
 & - \overbrace{\frac{F_2(A_t^i + 1)(-(k_1\alpha^{2k_1-2}(A_t^o + 1)) + \alpha^{2k_1}((k_1 + 1)A_t^o + k_1 - 1) + \alpha^{4k_1} - A_t^o)}{2(\alpha^{2k_1} - 1)(\alpha^{2k_1} + A_t^i A_t^o)}\dot{\eta}_{1,c1}^i}^{\text{Compressibility term III}} \\
 & - \overbrace{(A_t^i + 1)\frac{\alpha^{2k_1}(F_2^2 k_1(A_t^o + 1)R^i - F_2 \dot{R}^i(3k_1 A_t^o + A_t^o + 3k_1 - 1) - \dot{F}_2(A_t^o - 1)R^i)}{2(\alpha^{2k_1} - 1)R^i(\alpha^{2k_1} + A_t^i A_t^o)}\eta_{1,c1}^i}^{\text{Compressibility term IV}} \\
 & - \overbrace{(A_t^i + 1)\frac{-(F_2 k_1 \alpha^{2k_1-2}(A_t^o + 1)(F_2 R^i - 3\dot{R}^i)) + \alpha^{4k_1}(F_2 \dot{R}^i + \dot{F}_2 R^i) - A_t^o(F_2 \dot{R}^i + \dot{F}_2 R^i)}{2(\alpha^{2k_1} - 1)R^i(\alpha^{2k_1} + A_t^i A_t^o)}\eta_{1,c1}^i}^{\text{Compressibility term V}} \\
 & + \overbrace{\frac{F_2\alpha^{k_1-1}(A_t^i + 1)(\alpha^{2k_1+2}(A_t^o + k_1 + 1) - k_1\alpha^{2k_1} + \alpha^2((k_1 - 1)A_t^o - 1) - k_1 A_t^o)}{2(\alpha^{2k_1} - 1)(\alpha^{2k_1} + A_t^i A_t^o)}\dot{\eta}_{1,c1}^o}^{\text{Compressibility term VI}} \\
 & - \overbrace{(A_t^i + 1)\frac{\alpha^{k_1-1}(2F_2 \dot{R}^i((k_1 + 1)A_t^o + 1) + 2\dot{F}_2 k_1 A_t^o R^i - (F_2^2(A_t^o + 1)R^i))}{4(\alpha^{2k_1} - 1)R^i(\alpha^{2k_1} + A_t^i A_t^o)}\eta_{1,c1}^o}^{\text{Compressibility term VII}} \\
 & - \overbrace{(A_t^i + 1)\frac{\alpha^{k_1+1}(-2F_2 k_1 A_t^o \dot{R}^i + 2\dot{F}_2 R^i(-k_1 A_t^o + A_t^o + 1) + F_2^2(A_t^o + 1)R^i)}{4(\alpha^{2k_1} - 1)R^i(\alpha^{2k_1} + A_t^i A_t^o)}\eta_{1,c1}^o}^{\text{Compressibility term VIII}} \\
 & - \overbrace{(A_t^i + 1)\frac{\alpha^{3k_1-1}(-2F_2 \dot{R}^i(2k_1 A_t^o + A_t^o + k_1 + 1) - 2\dot{F}_2 k_1 A_t^o R^i + F_2^2(A_t^o + 1)R^i)}{4(\alpha^{2k_1} - 1)R^i(\alpha^{2k_1} + A_t^i A_t^o)}\eta_{1,c1}^o}^{\text{Compressibility term IX}}
 \end{aligned}$$

$$\begin{aligned}
 & - (A_t^i + 1) \frac{\alpha^{3k_1+1} (F_2^2 (k_1 - 1) (A_t^o + 1) R^i + 2 \dot{F}_2 R^i ((k_1 - 1) A_t^o - 1) - 2 F_2 k_1 \dot{R}^i)}{4 (\alpha^{2k_1} - 1) R^i (\alpha^{2k_1} + A_t^i A_t^o)} \eta_{1,c1}^o \\
 & \quad \text{Compressibility term X} \\
 & + (A_t^i + 1) \frac{F_2 k_1 \alpha^{3k_1-3} (A_t^o + 1) (F_2 R^i - 4 \dot{R}^i)}{4 (\alpha^{2k_1} - 1) R^i (\alpha^{2k_1} + A_t^i A_t^o)} \eta_{1,c1}^o = 0
 \end{aligned} \tag{10}$$

Compressibility term XI

and

$$\begin{aligned}
 & \overbrace{\ddot{\eta}_{1,c1}^o + 2 \frac{\dot{R}^o}{R^o} \dot{\eta}_{1,c1}^o}^{\text{BP term}} + \overbrace{(1 - k_1 A_t^o) \frac{\ddot{R}^o}{R^o} \eta_{1,c1}^o}^{\text{RT term}} + k_1 \overbrace{\frac{\alpha^{2k_1} (\alpha^2 - 1) (A_t^i - 1) (A_t^o - 1) \dot{R}^o}{(\alpha^{2k_1} - 1) (\alpha^{2k_1} + A_t^i A_t^o)} \frac{\dot{R}^o}{R^o} \eta_{1,c1}^o}^{\text{Thin-shell correction I}} + k_1 \overbrace{\frac{A_t^i A_t^o (A_t^o - 1) \ddot{R}^o}{\alpha^{2k_1} + A_t^i A_t^o} \frac{\ddot{R}^o}{R^o} \eta_{1,c1}^o}^{\text{Thin-shell correction II}} \\
 & + k_1 \overbrace{\frac{\alpha^{2k_1} (\alpha^2 - 1) (A_t^o - 1) (A_t^i - 1) (\dot{R}^o)^2}{(\alpha^{2k_1} - 1) (\alpha^{2k_1} + A_t^i A_t^o) (R^o)^2} \eta_{1,c1}^o}^{\text{Thin-shell corrections III}} - k_1 \overbrace{\frac{\alpha^{3k_1+1} (\alpha^2 - 1) (A_t^i - 1) (A_t^o - 1) (\dot{R}^o)^2}{(\alpha^{2k_1} - 1) (\alpha^{2k_1} + A_t^i A_t^o) (R^o)^2} \eta_{1,c1}^o}^{\text{Coupling term I}} \\
 & + k_1 \overbrace{\frac{\alpha^{k_1-1} (\alpha^2 - 1) (\alpha^{2k_1} - A_t^i) (A_t^o - 1) \dot{R}^o}{(\alpha^{2k_1} - 1) (\alpha^{2k_1} + A_t^i A_t^o) R^o} \dot{\eta}_{1,c1}^i}^{\text{Coupling term II}} + k_1 \overbrace{\frac{\alpha^{k_1+1} A_t^i (A_t^o - 1) \dot{R}^o}{\alpha^{2k_1} + A_t^i A_t^o} \frac{\dot{R}^o}{R^o} \eta_{1,c1}^i} \\
 & - \overbrace{\frac{\alpha^{k_1-1} (A_t^i - 1) (A_t^o - 1) (\alpha^2 \dot{F}_1 R^o + F_1 \dot{R}^o)}{2 (\alpha^{2k_1} + A_t^i A_t^o) R^i} \eta_{1,c1}^i - \frac{(A_t^o + 1) (\alpha^{2k_1} + A_t^i) (F_3 R^o + F_3 \dot{R}^o)}{2 (\alpha^{2k_1} + A_t^i A_t^o) R^o} \eta_{1,c1}^o}^{\text{Compressibility term I}} \\
 & - \overbrace{\frac{F_1 \alpha^{k_1-1} (A_t^o - 1) (A_t^i - 1)}{2 (\alpha^{2k_1} + A_t^i A_t^o)} \dot{\eta}_{1,c1}^i - \frac{F_3 (A_t^o + 1) (\alpha^{2k_1} + A_t^i)}{2 (\alpha^{2k_1} + A_t^i A_t^o)} \dot{\eta}_{1,c1}^o}^{\text{Compressibility term II}} \\
 & - \overbrace{\frac{F_2 \alpha^{k_1-1} (A_t^o - 1) (- (\alpha^{2k_1} (A_t^i + k_1 - 1)) + k_1 \alpha^{2k_1+2} - \alpha^2 k_1 A_t^i + (k_1 + 1) A_t^i - 1)}{2 (\alpha^{2k_1} - 1) (\alpha^{2k_1} + A_t^i A_t^o)} \dot{\eta}_{1,c1}^i}^{\text{Compressibility term III}} \\
 & - \overbrace{\alpha^{k_1-1} (A_t^o - 1) \frac{(\alpha^2 - 1) F_2^2 ((k_1 + 1) \alpha^{2k_1} + k_1 \alpha^{2k_1+2} - 1) (A_t^i - 1)}{4 (\alpha^{2k_1} - 1) (\alpha^{2k_1} + A_t^i A_t^o)} \eta_{1,c1}^i}^{\text{Compressibility term IV}} \\
 & + \overbrace{\alpha^{k_1-1} (A_t^o - 1) \frac{F_2 \dot{R}^o \alpha^{2k_1+2} (- 2 k_1 A_t^i + A_t^i + k_1 - 1)}{2 (\alpha^{2k_1} - 1) R^o (\alpha^{2k_1} + A_t^i A_t^o)} \eta_{1,c1}^i}^{\text{Compressibility term V}} \\
 & - \overbrace{\alpha^{k_1-1} (A_t^o - 1) \frac{2 F_2 \dot{R}^o k_1 \alpha^{2k_1+4} (A_t^i - 1) + F_2 \dot{R}^o k_1 \alpha^{2k_1} + F_2 \dot{R}^o \alpha^2 ((k_1 - 1) A_t^i + 1) - F_2 \dot{R}^o k_1 A_t^i}{2 (\alpha^{2k_1} - 1) R^o (\alpha^{2k_1} + A_t^i A_t^o)} \eta_{1,c1}^i}^{\text{Compressibility term VI}} \\
 & + \overbrace{\alpha^{k_1-1} (A_t^o - 1) \frac{\dot{F}_2 (\alpha^{2k_1} - 1) ((\alpha^2 k_1 - k_1 - 1) A_t^i + 1)}{2 (\alpha^{2k_1} - 1) (\alpha^{2k_1} + A_t^i A_t^o)} \eta_{1,c1}^i}^{\text{Compressibility term VII}} \\
 & + \overbrace{\frac{F_2 (A_t^o - 1) (\alpha^{2k_1} ((k_1 - 1) A_t^i - k_1 - 1) - k_1 \alpha^{2k_1+2} (A_t^i - 1) + \alpha^{4k_1} + A_t^i)}{2 (\alpha^{2k_1} - 1) (\alpha^{2k_1} + A_t^i A_t^o)} \dot{\eta}_{1,c1}^o}^{\text{Compressibility term VIII}}
 \end{aligned}$$

$$\begin{aligned}
& - (A_t^o - 1) \frac{\alpha^{2k_1} (F_2^2 k_1 (A_t^i - 1) R^o + F_2 \dot{R}^o (-3k_1 A_t^i + A_t^i + 3k_1 + 1) + \dot{F}_2 (A_t^i + 1) R^o)}{2(\alpha^{2k_1} - 1) R^o (\alpha^{2k_1} + A_t^i A_t^o)} \eta_{1,c1}^o \\
& \quad \text{Compressibility term IX} \\
& + (A_t^o - 1) \frac{F_2 k_1 \alpha^{2k_1+2} (A_t^i - 1) (F_2 R^o - 3\dot{R}^o)}{2(\alpha^{2k_1} - 1) R^o (\alpha^{2k_1} + A_t^i A_t^o)} \eta_{1,c1}^o \\
& \quad \text{Compressibility term X} \\
& + (A_t^o - 1) \frac{\alpha^{4k_1} (F_2 \dot{R}^o + \dot{F}_2 R^o) + A_t^i (F_2 \dot{R}^o + \dot{F}_2 R^o)}{2(\alpha^{2k_1} - 1) R^o (\alpha^{2k_1} + A_t^i A_t^o)} \eta_{1,c1}^o = 0, \tag{11} \\
& \quad \text{Compressibility term XI}
\end{aligned}$$

where $A_t^i = (\rho_2 - \rho_1)/(\rho_2 + \rho_1)$ is the Atwood number at inner interface. The driving forces for the growth of perturbations are divided into five categories similar to Ref. [30]. The BP term is attributed to the acceleration effect of geometric convergence and the RT term is attributed to the interfacial acceleration. The coupling effect between interfaces is represented by the two coupling terms, which are roughly proportional to α^{-k_1} for large α . The thin-shell corrections play a significant role when $\alpha \rightarrow 1$ and their contribution quickly decreases on the order of α^{-2k_1} with increasing α . At the thick-shell limit $\alpha \rightarrow \infty$, both coupling terms and thin-shell corrections can be neglected. Since the compressibility of fluid 1, i.e., of the innermost fluid, are represented by F_1 and \dot{F}_1 , which appear in the coefficients of $\eta_{1,c1}^i$ and $\dot{\eta}_{1,c1}^i$ at both inner and outer interfaces, its effects are negligible at the early stage of the compression, when both $\eta_{1,c1}^i$ and $\dot{\eta}_{1,c1}^i$ are still small.

The linearized governing equations of the sine mode of k_1 , i.e., $\eta_{1,s1}^{i,o}$, and both the sine and cosine modes of k_2 , i.e., $\eta_{1,c2}^{i,o}$ and $\eta_{1,s2}^{i,o}$, have the same form as those in Eqs. (10) and (11), and thus do not need to consider separately.

C. Mode-coupled weakly nonlinear instability and justification of the model

When one keeps higher-order ε terms of velocity potentials in Eqs. (7)–(9) and solves Eqs. (3) and (4) order by order with respect to ε , a mode-coupled weakly nonlinear solution can also be achieved in a similar way as getting the linear solution. Details of the mode-coupled weakly nonlinear solution up to the third-order of ε together with the corresponding higher-order expressions of velocity potentials can be found in the Supplemental Material [65]. The fourth- or higher-order terms are not kept as they turn out to have negligible effects to account for experiments even at the final stage of the measurements [66].

It should be stressed that in our mode-coupled weakly nonlinear solution, only higher-order modes of the two fundamental modes and induced modes caused by the interaction between the two fundamental modes are considered, as shown in Eq. (6). The validity of this treatment is not obvious considering other modes are also unstable and grow simultaneously during the cylindrical implosion. The validity is based on the assumption that perturbations of other modes are sufficiently small initially, so they keep small enough (compared to the

two fundamental modes and induced higher-order modes) during the experimental period, taking into consideration the fact that their amplitudes also grow with time. As we shall show in the next section, this assumption is justified by the experimental results *a posteriori*.

To provide an additional examination of the validity of our mode-coupled weakly nonlinear model, we also apply the model to a two-dimensional two-phase incompressible cylindrical implosion process, with both reference flow and the evolution of perturbations calculated using classical numerical hydrodynamical simulation, where initial perturbations of mode $k = 4$ and $k = 10$ are added in the outer interfaces of a ring-shaped liquid layer, and the implosion of the entire system consists of an acceleration and a deceleration stage, similar to the experimental configuration of Hsing *et al.* [43], but with a simplified treatment to the initial and boundary conditions. Our results show that the model is capable of capturing the main feature of the nonlinear evolution of multimode perturbations with mode-mode interaction. Details of the simulation and comparison with our model can be found in the Supplemental Material [65].

III. COMPARISON WITH THE EXPERIMENT

A. Reference flow and initial perturbations

To have a close comparison with experimental results [43], the reference flow has to be determined first. It amounts to determining $R^o(t)$, $R^i(t)$, $A_t^i(t)$, and $A_t^o(t)$. In the experiment, the middle layer, i.e., fluid 2 in Fig. 1, consisted of dichlorostyrene ($C_8H_6Cl_2$), which was less transparent to the x-ray back-lighter than adjacent layers. So, the trajectories of $R^o(t)$ and $R^i(t)$ were recorded as the average radii of the outer and inner boundaries of the middle layer, respectively, as displayed in Fig. 2(a) as triangular markers. In the theoretical calculations, fitted $R^o(t)$ and $R^i(t)$ of the experimental values are used, as shown as solid curves in Fig. 2(a), which help determine the time derivatives $\dot{R}^{i,o}(t)$ and $\dot{R}^{i,o}(t)$ for both interfaces, together with the parameter $\alpha(t)$ accounting for the degree of coupling between the two interfaces.

Figure 2(b) displays the evolution of α^k for the two fundamental modes $k_1 = 10$ and $k_2 = 4$ with the criterion of $\alpha^k = 36$ (dashed horizontal line, which is considered as the threshold of whether coupling between inner and outer interfaces for the given mode should be kept according to Zhang *et al.* [30]). Figure 2(b) shows that the decoupling of mode

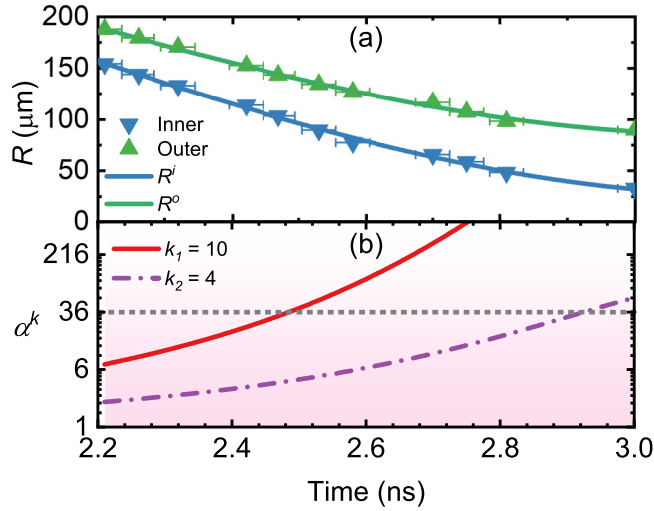


FIG. 2. (a) The recorded values of inner and outer radii from Ref. [43] and fitted trajectories $R^i(t)$ and $R^o(t)$ versus time. (b) The evolution of α^{k_1} and α^{k_2} , where $\alpha = R^o/R^i$. k_1 and k_2 are wave numbers of the modes. α^k is an indication of the coupling strength between two interfaces. Note that the coupling strength is inversely proportional to the value of α^k . The position of $\alpha^k = 36$, which is the threshold to regard two interfaces as not coupled, is marked with a dashed horizontal line. The shade of the pink background represents the strength of the coupling.

$k_1 = 10$ takes place at $t \approx 2.48$ ns, and at $t \approx 2.93$ ns for mode $k_2 = 4$, which suggests that coupling effects between the two interfaces shall play important roles for the evolution of perturbations.

Then, $\rho_1(t)$ of the inner fluid, i.e., fluid 1 in Fig. 1, is determined from $R^i(t)$, and the $\rho_2(t)$ is determined from $R^i(t)$ and $R^o(t)$ with the assumption of uniform compression. Note that initially $R^i(t = 2.21) = 155.02 \mu\text{m}$, $R^o(t = 2.21) = 188.38 \mu\text{m}$, $\rho_1(t = 2.21) = 0.45 \text{ g/cc}$, and $\rho_2(t = 2.21) = 0.8 \text{ g/cc}$. Here, $t = 2.21$ ns is the initial time of the experimental recording and also the initial time of the theoretical calculation. With these two densities, $A_i^i(t)$ can be readily calculated through $A_i^i(t) = [\rho_2(t) - \rho_1(t)]/[\rho_2(t) + \rho_1(t)]$. It was difficult to determine $\rho_3(t)$ in experiments because its density varied significantly along the radial axis. However, as was revealed by Hsing *et al.* [43] through hydrodynamic simulations, the ratio of ρ_2 and ρ_3 at the interface was kept roughly a constant, and so was the Atwood number during the observation period, i.e., from about 2.21 ns to 3 ns. So, we take $A_i^o(t) \sim -0.15$ here, following experimental results.

Since the experimental data were not recorded from the beginning of the experiment, i.e., not from $t = 0$, as displayed in Fig. 2(a), one has to figure out $\eta_{\alpha,\beta}^{i,o}$ and their derivatives $\dot{\eta}_{\alpha,\beta}^{i,o}$ at the time when the data started to record and use them as initial conditions to advance the calculation of $\eta_{\alpha,\beta}^{i,o}$, e.g., in linear stability analysis, $\eta_{1,c1}^{i,o}(t)$ in Eqs. (10) and (11). To get the initial conditions, we first extract the two boundaries $r^{i,o}(\theta)$ of the middle fluid layer in the first recorded x-ray image (at $t = 2.21$ ns) as displayed in Fig. 3(a) with dashed curves, and then expand them as Fourier series in the form of $r^{i,o}(\theta) = R^{i,o} + \sum_m a_m \cos(m\theta) + b_m \sin(m\theta)$. The $\eta_{\alpha,\beta}^{i,o}$ are

determined as the coefficients of the corresponding modes included in Eq. (6).

The derivatives $\dot{\eta}_{\alpha,\beta}^{i,o}$ are obtained with the help of the second recorded x-ray image at $t = 2.26$ ns, as displayed in Fig. 3(b), where $\eta_{\alpha,\beta}^{i,o}$ are first determined in the same way as for the first x-ray image, and then the derivatives are obtained from the differences $\Delta\eta_{\alpha,\beta}^{i,o}/\Delta t$ of the two images in a finite difference style. Considering that the measurement of $\Delta\eta_{\alpha,\beta}^{i,o}$ usually suffers from large random errors, a small adjustment to $\Delta\eta_{\alpha,\beta}^{i,o}$ may also be added manually to make the calculation result reasonable. A complete list of $\eta_{\alpha,\beta}^{i,o}$ and their derivatives $\dot{\eta}_{\alpha,\beta}^{i,o}$ can be found in the Supplemental Material [65].

B. Evolution of perturbations

With all the above issues settled, the time development of $\eta_{\alpha,\beta}^{i,o}$ can be integrated with a second-order center-difference scheme. Figure 3 displays calculated evolution profiles of the perturbation from $t = 2.21$ ns to $t = 3.05$ ns, which covers the entire recording period of the experiment. The experimental images for both inner and outer interfaces are also plotted for reference. It shows that theoretical results well follow the experimental measurements until $t > 2.81$ ns. In the period from $t = 2.21$ ns to $t = 2.53$ ns, the outer interface is dominated by the perturbation of the $k = 10$ mode. The perturbation of the $k = 4$ mode becomes visible from $t = 2.58$ ns, and its amplitude is comparable with that of the $k = 10$ mode at the final stage of the recording from about $t = 2.75$ ns. In contrast, the perturbation on the inner interface mainly contains the $k = 4$ fundamental mode, which is visible at the early stage from $t = 2.42$ ns.

The fundamental mode of $k = 10$, which is dominant on the outer interface, however, has a small amplitude on the inner interface at the beginning of the recording period and fades out quickly from around $t = 2.32$ ns. It is also interesting to notice that the $k = 2$ mode becomes visible on the inner interface near the final stage of the recording, starting from $t = 2.70$ ns, as can be seen from the elongation of the inner interface along the vertical direction, whereas on the outer interface, the amplitude of the $k = 2$ mode stays small compared to the two, i.e., $k = 4$ and $k = 10$, fundamental modes. It should be noted that the calculated profiles presented in Fig. 3 do not exactly agree with the experimental profiles since only fundamental modes and their intercoupling modes are kept in the theoretical model. The differences mainly come from the neglect of odd modes, which are not prominent in the experiment because the fundamental modes and their intercoupling modes have much larger amplitudes which dominate the perturbation profiles.

At the final stage, starting from $t = 3.00$ ns, Fig. 3 shows that theoretical results severely deviate from experimental results. In particular, the perturbation amplitude on the outer interface is much overestimated by the weakly nonlinear model compared to the experimental measurements. This is within the expectation on the performance of the weakly nonlinear model, since from around $t = 3.00$ ns, the implosion is at the stagnation stage, where the growth of perturbation amplitudes is prominently affected by complicated interaction between bouncing shock fronts and interfaces, and is thus far beyond the scope of weakly nonlinear models.

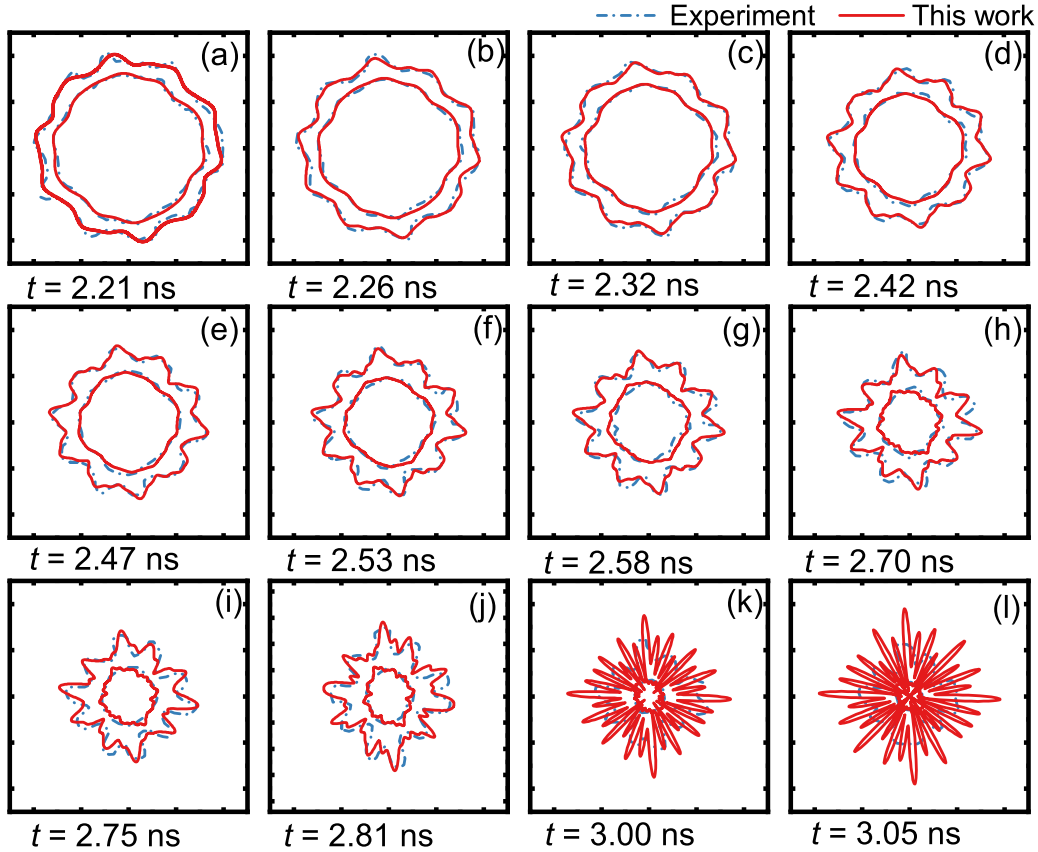


FIG. 3. The evolution of perturbations on inner and outer interfaces at different moments. The red solid lines are calculated from our weakly nonlinear model, and the blue dot-dashed lines are extracted from x-ray images in Ref. [43]. The agreement between the mode-coupled weakly nonlinear model and experimental measurements can be observed in (a)–(j) before $t = 3.00$ ns. In (k) and (l), the weakly nonlinear model has a severe deviation from the experiment at the final stagnation stage, as a result of the incompleteness of describing highly nonlinear effects at the stagnation stage.

To justify the theoretical model, which only keeps the $k = 10$ and $k = 4$ fundamental modes and their higher harmonic terms up to the third order, Fig. 4 displays the Fourier decomposition of the inner and outer interfaces as the function of wave number m at the initial time $t = 2.21$ ns and an intermediate time $t = 2.47$ ns. The amplitudes displayed in the figure are the root-mean-square of the coefficients of both the sine and cosine components of the mode. The horizontal dashed line displays the noise level of the experimental measurements [43]. Figure 4 shows that the model predictions agree well with experiments, showing that our model captures the essence of the perturbation evolution.

Figure 5 displays a decomposition of perturbation amplitudes for the $k = 4$ and 10 modes on both outer and inner interfaces, where triangles are amplitudes extracted from Fig. 3 through Fourier expansion, and solid curves are results calculated from the weakly nonlinear model. As a comparison, the perturbation amplitudes from the linear terms, i.e., the first order terms in Eq. (6) with respect to ε , are also plotted in the figure as dashed curves.

On the outer interface, the growth of perturbation amplitudes, especially that of the $k = 10$ mode, displays the necessity to include nonlinearity in the model. As shown in Fig. 5(a), the amplitude of the $k = 10$ mode on the outer

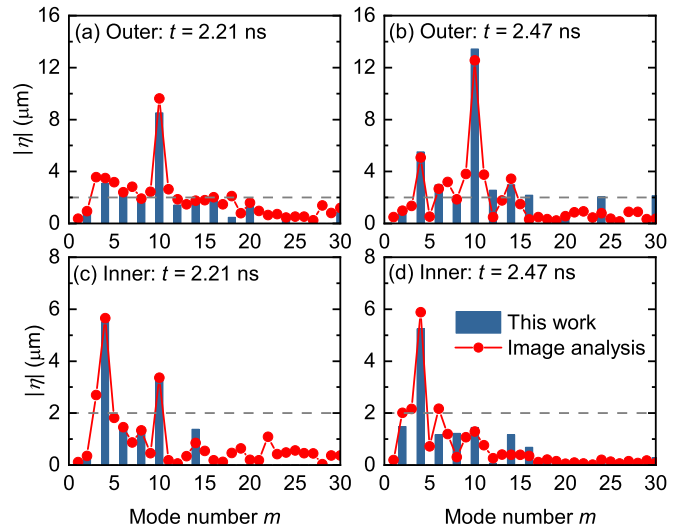


FIG. 4. The Fourier decomposition of (a) outer interface at $t = 2.21$ ns, (b) outer interface at $t = 2.47$ ns, (c) inner interface at $t = 2.21$ ns, and (d) inner interface at $t = 2.47$ ns. The gray dashed line is the noise threshold in the experimental measurements [43]. The bars are the results of our mode-coupled nonlinear model, and red dots are extracted from x-ray images of the experiments [43].

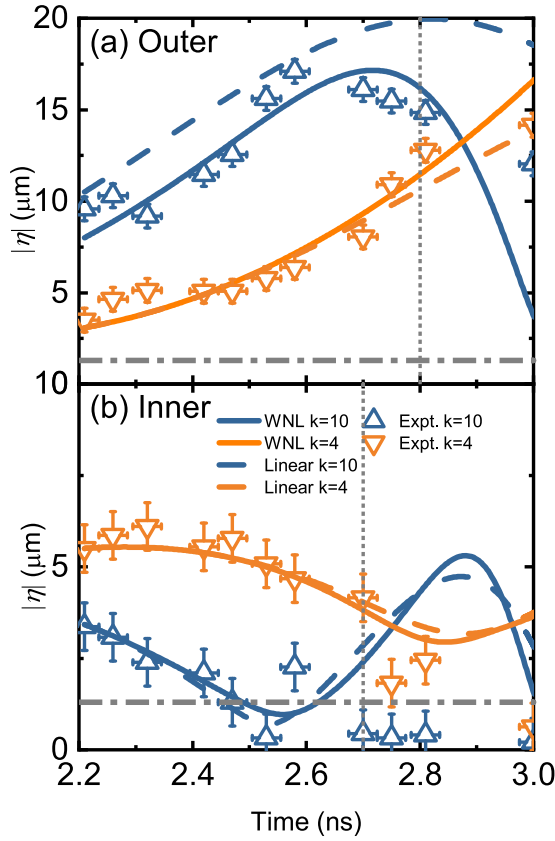


FIG. 5. The perturbation amplitudes of the fundamental modes $k = 4$ and $k = 10$ on (a) the outer interface and (b) inner interface. The triangles represent the amplitudes extracted from x-ray images in Ref. [43] through Fourier expansion, and the solid and dashed lines represent the mode-coupled weakly nonlinear model results and linear contributions, respectively. The vertical dashed lines at $t = 2.7$ ns in (a) and $t = 2.8$ ns in (b) indicate the moments when the first reflected shock wave from the cylindrical center arrives at the interfaces. The horizontal dash-dotted line shows the noise level in the experimental measurements.

interface reaches its maximum at around $t = 2.7$ ns and then displays a fast decrease. This amplitude evolution feature results from the combination of $\eta_{1,c1}^o(t)$ and $\eta_{3,c3}^o(t)$ in Eq. (6), which are the linear amplitude components of the $k = 10$ mode and the third-order nonlinear contribution, respectively. The third-order nonlinear term provides the necessary decreasing mechanism and determines the position of the peak together with the rate of decreasing. Without nonlinearity, however, the amplitude stays in the increasing phase for a much longer time, as shown by the dashed curve, and the experimental feature will not be recovered.

The second-order harmonic modes $k = 6, 8$, and 14 on the outer interface are displayed in Fig. 6(a) and the third-order coupled modes $k = 2$ and 12 are displayed in Fig. 7(a). It is not easy to recognize these modes by eye from the recorded profiles in Fig. 3 because the amplitude of the $k = 10$ fundamental mode is much larger than the amplitudes of these modes, as shown by the comparisons in Figs. 6(a) and 7(a), where the fundamental modes are displayed as a tinted background. However, the evolution of these modes can still be demonstrated by the Fourier decomposition. As displayed in

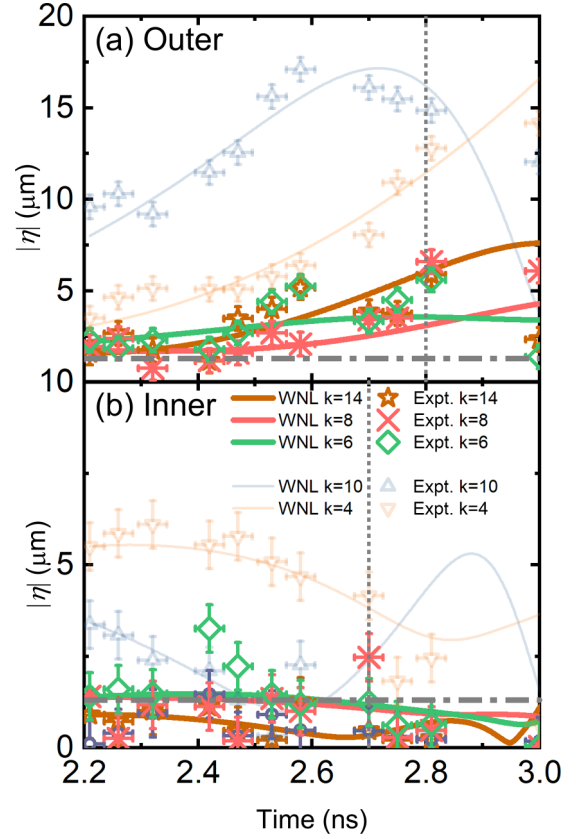


FIG. 6. The perturbation amplitudes for the second-order modes $k = 6, 8$, and 14 on (a) the outer interface and (b) the inner interface. The markers with error bars represent the amplitudes extracted from x-ray images in Ref. [43] through Fourier expansion, and the solid lines represent the results calculated from our mode-coupled weakly nonlinear model. The vertical dashed lines at $t = 2.7$ ns in (a) and $t = 2.8$ ns in (b) indicate the moments when the first reflected shock wave from the cylindrical center arrives at the interfaces. The horizontal dash-dotted line shows the noise level in the experimental measurements. The results of the fundamental modes are plotted as a tinted background.

Fig. 6(a), in addition to the much smaller amplitudes, the growth rates of the second harmonic modes are also much smaller than those of fundamental modes. Compared with the second-order harmonic modes, the third-order harmonic $k = 2$ and 14 modes on the outer interface are negligibly small. As shown in Fig. 7(a), their amplitudes fluctuate around the noise level (the horizontal dash-dotted line). On the inner interface, two prominent features can be recognized from Fig. 3 by eye. One is the diminishing of the $k = 4$ and $k = 10$ fundamental modes and the other is the increasing of the $k = 2$ harmonic mode before $t = 2.81$ ns. They turn out to come from different origins. The diminishing of the $k = 4$ and $k = 10$ fundamental modes before $t = 2.81$ ns is dominated by the linear evolution effect, as illustrated by the comparison between the perturbation evolution with and without nonlinear terms in Fig. 5(b). This decrease is attributed to the takeover of the oscillatory evolution of the coupled inner and outer interfaces during the transition stage of the implosion, i.e., the time period characterized by $6 < \alpha^k < 36$ [30]. As revealed in Ref. [30], it is a common feature of two coupled interfaces that

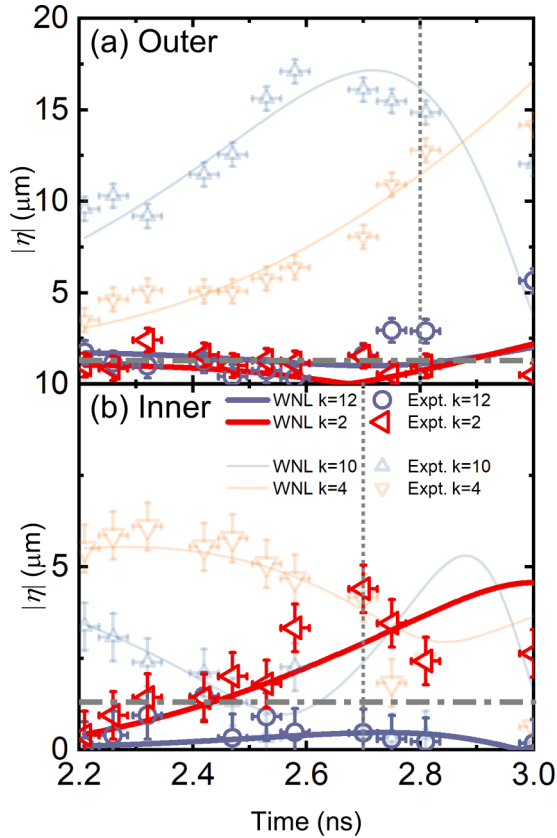


FIG. 7. The perturbation amplitudes for the third-order modes $k = 2$ and 12 on (a) the outer interface and (b) the inner interface. The markers with error bars represent the amplitudes extracted from x-ray images in Ref. [43] through Fourier expansion, and the solid lines represent the results calculated from our mode-coupled weakly nonlinear model. The vertical dashed lines at $t = 2.7$ ns in (a) and $t = 2.8$ ns in (b) indicate the moments when the first reflected shock wave from the cylindrical center arrives at the interfaces. The horizontal dash-dotted line shows the noise level in the experimental measurements. The results of the fundamental modes are plotted as a tinged background.

the most unstable mode is overtaken by the previous second oscillatory unstable mode at the transition stage, and the previous most unstable mode becomes the second unstable mode. Before $t = 2.81$ ns, the $k = 4$ and $k = 10$ fundamental modes are in the decreasing phase of an oscillatory period (where the amplitude keeps decreasing but the acceleration is positive) and thus display the decreasing tendency. It should be noted that the amplitudes of the two modes would eventually grow up if the instability was not interrupted by other events, as shown by the theoretical curves in Fig. 5(b).

The amplitudes of the second harmonic modes on the inner interface fluctuate around $2 \mu\text{m}$, which is slightly above the noise level, as displayed in Fig. 6(b). In addition, our mode-coupled nonlinear model shows that the amplitudes tend to decay slowly. The third-order harmonic modes of $k = 2$ and 12 on the inner interface exhibit different features. The behavior of the $k = 12$ mode is similar to the behavior of the second harmonic modes, but with an even smaller amplitude, as displayed in Fig. 7(b). However, the $k = 2$ mode on the inner interfaces gradually grows up. Although its am-

plitude is not large, i.e., less than $5 \mu\text{m}$, during the recording period the amplitude is comparable with the amplitude of the fundamental $k = 4$ mode at around $t = 2.7$ ns, as displayed in Fig. 7(b), and thereby easy to recognize in Figs. 3(i) and 3(j) as a feature of a vertical elongation of the profile.

The growth of the third harmonic mode $k = 2$ suggests that the energy of the fundamental $k = 4$ and $k = 10$ modes, i.e., the small-scale modes, is transferred to the $k = 2$ mode, i.e., the large-scale mode, through nonlinear mode-mode interaction, forming an inverse cascade in the mode space. The inverse cascade was also revealed in recent numerical simulations and experiments of two-dimensional converging implosions [67–69], and was illustrated in magnetic-RT instability experiments along the axial direction [70,71]. Since the $k = 2$ mode is induced by higher wave number modes, it may pose interesting problems for the prevention or control of the appearance of lower wave number modes in future experimental and theoretical investigations, as they have the potential of further reducing the energy gain of ICF implosion [55].

There are abrupt changes observed on both interfaces in the evolution of perturbation amplitudes. On the inner interface, the change takes place at around $t = 2.7$ ns, while the change appears at around $t = 2.8$ ns on the outer interface. Both moments are shown as vertical dotted lines in Fig. 5. After these moments, the weakly nonlinear calculations deviate from the perturbation amplitudes measured in experiments. The time $t = 2.7$ ns and $t = 2.8$ ns are the moments when the first reflected shock wave from the center meets the two interfaces, as revealed in a separate hydrodynamic simulation. From $t = 2.8$ ns, the system enters the stagnation stage, dominated by successive reflections of shock waves between the cylindrical center and the two interfaces. So, it is expected that the weakly nonlinear model becomes ineffective after $t = 2.8$ ns.

IV. SUMMARY

In summary, we provide a mode-coupled weakly nonlinear model to account for perturbation evolution in multi-interface cylindrical implosion. We find that compression effects, interfacial coupling, and weakly nonlinear effects are necessary ingredients for a satisfactory description of the perturbation development. A close comparison with experimental measurements shows that our model captures important features of multishell cylindrical implosion near the stagnation. In particular, we show that the inverse cascade in the mode space is able to excite small wave-number modes, which may bring about interesting problems for the prevention or control of these small wave-number modes. In addition, the interfacial coupling effect induced oscillatory growth affords an alternative physical picture for the perturbation evolution in cylindrical implosion. These results may help gain further insight into the distortion of hot spots in ICF implosion and may also provide direct assistance to the design of cylindrical multimode experiments in the future.

ACKNOWLEDGMENTS

We acknowledge J. Shen for the insightful discussions. This work was financially supported by the Fundamental Research Funds for the Central Universities, Peking University.

- [1] L. Rayleigh, *Proc. London Math. Soc.* **s1-14**, 170 (1882).
- [2] G. I. Taylor, *Proc. R. Soc. London A* **201**, 192 (1950).
- [3] S. Chandrasekhar, *Hydrodynamic and Hydromagnetic Stability* (Dover Publications, New York, 1981).
- [4] S. P. Regan, J. A. Delettrez, V. N. Goncharov, F. J. Marshall, J. M. Soures, V. A. Smalyuk, P. B. Radha, B. Yaakobi, R. Epstein, V. Y. Glebov, P. A. Jaanimagi, D. D. Meyerhofer, T. C. Sangster, W. Seka, S. Skupsky, C. Stoeckl, D. A. Haynes, Jr., J. A. Frenje, C. K. Li, R. D. Petrasso, and F. H. Séguin, *Phys. Rev. Lett.* **92**, 185002 (2004).
- [5] H.-S. Park, O. A. Hurricane, D. A. Callahan, D. T. Casey, E. L. Dewald, T. R. Dittrich, T. Döppner, D. E. Hinkel, L. F. Berzak Hopkins, S. Le Pape, T. Ma, P. K. Patel, B. A. Remington, H. F. Robey, J. D. Salmonson, and J. L. Kline, *Phys. Rev. Lett.* **112**, 055001 (2014).
- [6] R. S. Craxton, K. S. Anderson, T. R. Boehly, V. N. Goncharov, D. R. Harding, J. P. Knauer, R. L. McCrory, P. W. McKenty, D. D. Meyerhofer, J. F. Myatt, A. J. Schmitt, J. D. Sethian, R. W. Short, S. Skupsky, W. Theobald, W. L. Kruer, K. Tanaka, R. Betti, T. J. B. Collins, J. A. Delettrez *et al.*, *Phys. Plasmas* **22**, 110501 (2015).
- [7] K. Lan, *Matter Radiat. Extremes* **7**, 055701 (2022).
- [8] A. L. Kritcher, C. V. Young, H. F. Robey, C. R. Weber, A. B. Zylstra, O. A. Hurricane, D. A. Callahan, J. E. Ralph, J. S. Ross, K. L. Baker, D. T. Casey, D. S. Clark, T. Döppner, L. Divol, M. Hohenberger, L. B. Hopkins, S. Le Pape, N. B. Meezan, A. Pak, P. K. Patel *et al.*, *Nat. Phys.* **18**, 251 (2022).
- [9] O. A. Hurricane, P. K. Patel, R. Betti, D. H. Froula, S. P. Regan, S. A. Sclutz, M. R. Gomez, and M. A. Sweeney, *Rev. Mod. Phys.* **95**, 025005 (2023).
- [10] K. Batani, D. Batani, X. T. He, and K. Shigemori, *Matter Radiat. Extremes* **7**, 013001 (2022).
- [11] B. Albertazzi, P. Mabey, T. Michel, G. Rigon, J. R. Marquès, S. Pikuz, S. Ryazantsev, E. Falize, L. Van Box Som, J. Meinecke, N. Ozaki, G. Gregori, and M. Koenig, *Matter Radiat. Extremes* **7**, 036902 (2022).
- [12] W. Yao, J. Capitaine, B. Khair, T. Vinci, K. Burdonov, J. Béard, J. Fuchs, and A. Ciardi, *Matter Radiat. Extremes* **7**, 026903 (2022).
- [13] N. E. Lanier, J. Workman, R. L. Holmes, P. Graham, and A. Moore, *Phys. Plasmas* **14**, 056314 (2007).
- [14] T. R. Dittrich, O. A. Hurricane, D. A. Callahan, E. L. Dewald, T. Döppner, D. E. Hinkel, L. F. Berzak Hopkins, S. Le Pape, T. Ma, J. L. Milovich, J. C. Moreno, P. K. Patel, H.-S. Park, B. A. Remington, J. D. Salmonson, and J. L. Kline, *Phys. Rev. Lett.* **112**, 055002 (2014).
- [15] R. E. Olson, R. J. Leeper, J. L. Kline, A. B. Zylstra, S. A. Yi, J. Biener, T. Braun, B. J. Koziolowski, J. D. Sater, P. A. Bradley, R. R. Peterson, B. M. Haines, L. Yin, L. F. Berzak Hopkins, N. B. Meezan, C. Walters, M. M. Biener, C. Kong, J. W. Crippen, G. A. Kyrala *et al.*, *Phys. Rev. Lett.* **117**, 245001 (2016).
- [16] V. A. Smalyuk, C. R. Weber, O. L. Landen, S. Ali, B. Bachmann, P. M. Celliers, E. L. Dewald, A. Fernandez, B. A. Hammel, G. Hall, A. G. MacPhee, L. Pickworth, H. F. Robey, N. Alfonso, K. L. Baker, L. F. B. Hopkins, L. Carlson, D. T. Casey, D. S. Clark, J. Crippen *et al.*, *Plasma Phys. Control. Fusion* **62**, 014007 (2020).
- [17] J. Lindl, *Phys. Plasmas* **2**, 3933 (1995).
- [18] J. D. Lindl, P. Amendt, R. L. Berger, S. G. Glendinning, S. H. Glenzer, S. W. Haan, R. L. Kauffman, O. L. Landen, and L. J. Suter, *Phys. Plasmas* **11**, 339 (2004).
- [19] S. H. Glenzer, D. H. Froula, L. Divol, M. Dorr, R. L. Berger, S. Dixit, B. A. Hammel, C. Haynam, J. A. Hittinger, J. P. Holder, O. S. Jones, D. H. Kalantar, O. L. Landen, A. B. Langdon, S. Langer, B. J. MacGowan, A. J. Mackinnon, N. Meezan, E. I. Moses, C. Niemann *et al.*, *Nat. Phys.* **3**, 716 (2007).
- [20] V. A. Thomas and R. J. Kares, *Phys. Rev. Lett.* **109**, 075004 (2012).
- [21] J. Gu, Z. Dai, S. Zou, W. Ye, W. Zheng, P. Gu, and S. Zhu, *Matter Radiat. Extremes* **2**, 9 (2017).
- [22] X. Qiao and K. Lan, *Phys. Rev. Lett.* **126**, 185001 (2021).
- [23] K. O. Mikaelian, *Phys. Rev. Lett.* **48**, 1365 (1982).
- [24] D. L. Book and S. E. Bodner, *Phys. Fluids* **30**, 367 (1987).
- [25] H. J. Kull, *Phys. Rev. A* **41**, 4312 (1990).
- [26] K. O. Mikaelian, *Phys. Rev. Lett.* **65**, 992 (1990).
- [27] K. O. Mikaelian, *Phys. Fluids* **17**, 094105 (2005).
- [28] J. W. Jacobs and S. B. Dalziel, *J. Fluid Mech.* **542**, 251 (2005).
- [29] A. L. Velikovich and P. F. Schmit, *Phys. Plasmas* **22**, 122711 (2015).
- [30] S. Zhang, H. Liu, W. Kang, Z. Xiao, J. Tao, P. Zhang, W. Zhang, and X. T. He, *Phys. Rev. E* **101**, 023108 (2020).
- [31] M. Yuan, Z. Zhao, L. Liu, P. Wang, N.-S. Liu, and X.-Y. Lu, *J. Fluid Mech.* **969**, A6 (2023).
- [32] S. W. Haan, *Phys. Rev. A* **39**, 5812 (1989).
- [33] J. Garnier, P. A. Raviart, C. Cherfils-Clerouin, and L. Masse, *Phys. Rev. Lett.* **90**, 185003 (2003).
- [34] A. L. Velikovich, M. Herrmann, and S. I. Abarzhi, *J. Fluid Mech.* **751**, 432 (2014).
- [35] C. Zulick, Y. Aglitskiy, M. Karasik, A. J. Schmitt, A. L. Velikovich, and S. P. Obenschain, *Phys. Rev. Lett.* **125**, 055001 (2020).
- [36] L. Baker, *Phys. Fluids* **26**, 950 (1983).
- [37] R. Epstein, *Phys. Plasmas* **11**, 5114 (2004).
- [38] H. Yu and D. Livescu, *Phys. Fluids* **20**, 104103 (2008).
- [39] E. G. Harris, *Phys. Fluids* **5**, 1057 (1962).
- [40] Y. Y. Lau, J. C. Zier, I. M. Rittersdorf, M. R. Weis, and R. M. Gilgenbach, *Phys. Rev. E* **83**, 066405 (2011).
- [41] D. E. Ruiz, *Phys. Plasmas* **27**, 022121 (2020).
- [42] J. L. Dai, Y. B. Sun, C. Wang, R. H. Zeng, and L. Y. Zou, *Phys. Plasmas* **30**, 022704 (2023).
- [43] W. W. Hsing, C. W. Barnes, J. B. Beck, N. M. Hoffman, D. Galmiche, A. Richard, J. Edwards, P. Graham, S. Rothman, and B. Thomas, *Phys. Plasmas* **4**, 1832 (1997).
- [44] W. W. Hsing and N. N. Hoffman, *Phys. Rev. Lett.* **78**, 3876 (1997).
- [45] J. R. Fincke, N. E. Lanier, S. H. Batha, R. M. Hueckstaedt, G. R. Magelssen, S. D. Rothman, K. W. Parker, and C. J. Horsfield, *Phys. Rev. Lett.* **93**, 115003 (2004).
- [46] F. Lei, J. Ding, T. Si, Z. Zhai, and X. Luo, *J. Fluid Mech.* **826**, 819 (2017).
- [47] S. Palaniyappan, J. P. Sauppe, B. J. Tobias, C. F. Kawaguchi, K. A. Flippo, A. B. Zylstra, O. L. Landen, D. Shvarts, E. Malka, S. H. Batha, P. A. Bradley, E. N. Loomis, N. N. Vazirani, L. Kot, D. W. Schmidt, T. H. Day, R. Gonzales, and J. L. Kline, *Phys. Plasmas* **27**, 042708 (2020).
- [48] J. P. Sauppe, S. Palaniyappan, E. N. Loomis, J. L. Kline, K. A. Flippo, and B. Srinivasan, *Matter Radiat. Extremes* **4**, 065403 (2019).

- [49] J. P. Sauppe, S. Palaniyappan, J. L. Kline, K. A. Flippo, O. L. Landen, D. Shvarts, S. H. Batha, P. A. Bradley, E. N. Loomis, B. J. Tobias, N. N. Vazirani, C. F. Kawaguchi, L. Kot, D. W. Schmidt, T. H. Day, A. B. Zylstra, and E. Malka, *High Energy Density Phys.* **36**, 100831 (2020).
- [50] J. P. Sauppe, S. Palaniyappan, B. J. Tobias, J. L. Kline, K. A. Flippo, O. L. Landen, D. Shvarts, S. H. Batha, P. A. Bradley, E. N. Loomis, N. N. Vazirani, C. F. Kawaguchi, L. Kot, D. W. Schmidt, T. H. Day, A. B. Zylstra, and E. Malka, *Phys. Rev. Lett.* **124**, 185003 (2020).
- [51] C. Samulski, B. Srinivasan, M. J.-E. Manuel, R. Masti, J. P. Sauppe, and J. Kline, *Matter Radiat. Extremes* **7**, 026902 (2022).
- [52] R. Roycroft, J. P. Sauppe, and P. A. Bradley, *Phys. Plasmas* **29**, 032704 (2022).
- [53] G. I. Bell, Taylor instability on cylinders and spheres in the small amplitude approximation, Tech. Rep. No. LA-1321, Los Alamos National Laboratory, 1951.
- [54] M. S. Plesset, *J. Appl. Phys.* **25**, 96 (1954).
- [55] S. Atzeni and J. Meyer-ter-Vehn, *The Physics of Inertial Fusion: Beam-Plasma Interaction, Hydrodynamics, Hot Dense Matter* (Oxford University Press, Oxford, 2004).
- [56] K. O. Mikaelian, *Phys. Rev. E* **89**, 053009 (2014).
- [57] Y. Zhou, *Phys. Rep.* **723-725**, 1 (2017).
- [58] H. Li, B. Tian, Z. He, and Y. Zhang, *Phys. Rev. E* **103**, 053109 (2021).
- [59] D. L. Tubbs, C. W. Barnes, J. B. Beck, N. M. Hoffman, J. A. Oertel, R. G. Watt, T. Boehly, D. Bradley, P. Jaanimagi, and J. Knauer, *Phys. Plasmas* **6**, 2095 (1999).
- [60] L. F. Wang, J. F. Wu, H. Y. Guo, W. H. Ye, J. Liu, W. Y. Zhang, and X. T. He, *Phys. Plasmas* **22**, 082702 (2015).
- [61] Z. Zhao, P. Wang, N. Liu, and X. Lu, *J. Fluid Mech.* **900**, A24 (2020).
- [62] J. Wu, H. Liu, and Z. Xiao, *J. Fluid Mech.* **908**, A9 (2021).
- [63] Z. Wang, K. Xue, and P. Han, *Phys. Fluids* **33**, 034118 (2021).
- [64] J. Li, H. Wang, Z. Zhai, and X. Luo, *Phys. Fluids* **35**, 106112 (2023).
- [65] See Supplemental Material at <http://link.aps.org/supplemental/10.1103/PhysRevE.109.035203> for details of the weakly non-linear solution and Ref. [72] for the format of Mathematica files; Refs. [73–80] for simulation details; and complete list of initial parameters.
- [66] K. Nishihara and T. Ikegawa, *J. Plasma Fusion Res. Ser.* **2**, 536 (1999).
- [67] Z. Zhou, J. Ding, Z. Zhai, W. Cheng, and X. Luo, *Acta Mech. Sin.* **36**, 356 (2020).
- [68] J. Xu, H. Wang, Z. Zhai, and X. Luo, *J. Fluid Mech.* **965**, A8 (2023).
- [69] Y. Liang, L. Liu, X. Luo, and C.-Y. Wen, *J. Fluid Mech.* **963**, A25 (2023).
- [70] D. E. Ruiz, D. A. Yager-Elorriaga, K. J. Peterson, D. B. Sinars, M. R. Weis, D. G. Schroen, K. Tomlinson, J. R. Fein, and K. Beckwith, *Phys. Rev. Lett.* **128**, 255001 (2022).
- [71] X. Wang, X. Ren, S. Meng, C. Mao, D. Xiao, Q. Yi, S. Zhou, X. Huang, X. Zhou, W. Weng, Z. Huang, C. Xue, G. Wang, S. Sun, and X. Shu, *Nucl. Fusion* **63**, 106003 (2023).
- [72] W. R. Inc., Mathematica, Version 13.0, Champaign, IL, 2023.
- [73] J. Kim, *Commun. Comput. Phys.* **12**, 613 (2012).
- [74] H. Ding, P. D. M. Spelt, and C. Shu, *J. Comput. Phys.* **226**, 2078 (2007).
- [75] T. J. Baker, *Finite Elem. Anal. Des.* **25**, 243 (1997).
- [76] A. Balan, M. A. Park, S. L. Wood, W. K. Anderson, A. Rangarajan, D. P. Sanjaya, and G. May, *Comput. Fluids* **234**, 105259 (2022).
- [77] C. Hirsch, *Numerical Computation of Internal and External Flows: The Fundamentals of Computational Fluid Dynamics*, 2nd ed. (Butterworth-Heinemann, Oxford, 2007).
- [78] D. Kuzmin and J. Hämäläinen, *Finite Element Methods for Computational Fluid Dynamics: A Practical Guide* (Society for Industrial and Applied Mathematics, Philadelphia, PA, 2014).
- [79] J. N. Reddy, N. K. Anand, and P. Roy, *Finite Element and Finite Volume Methods for Heat Transfer and Fluid Dynamics* (Cambridge University Press, Cambridge, 2022).
- [80] J. W. Cahn and J. E. Hilliard, *J. Chem. Phys.* **28**, 258 (1958).